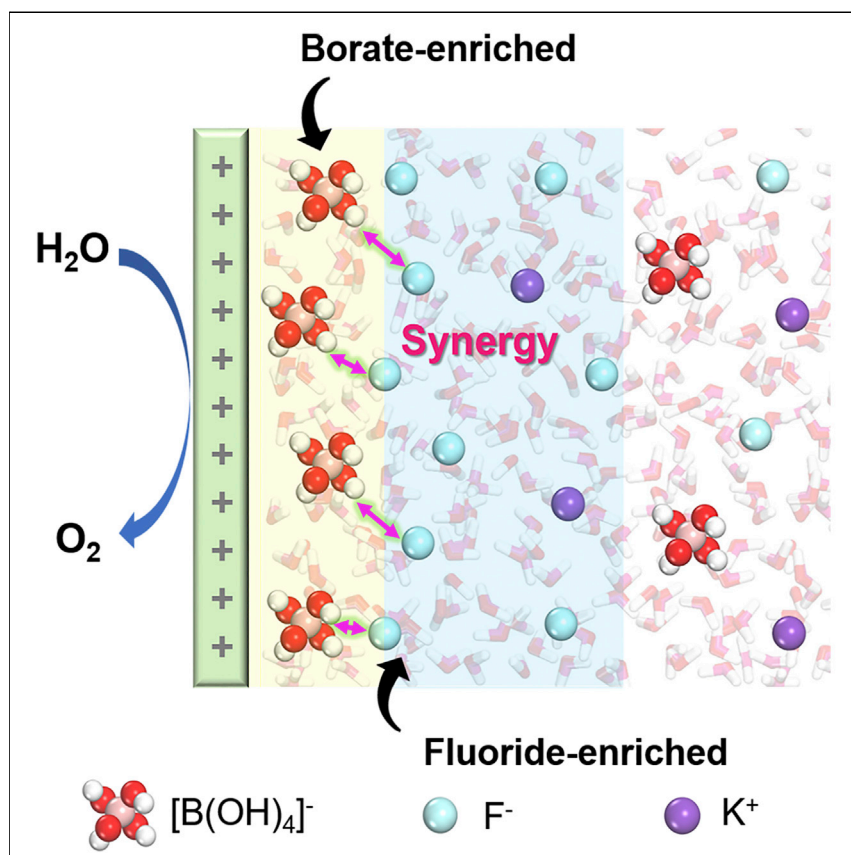


## Article

## Hierarchical anions at the electrode-electrolyte interface for synergized neutral water oxidation



The hierarchical borate and fluoride anion structure at the electrode-electrolyte interface creates a synergy for efficient neutral water oxidation.

Tao Liu, Yuxin Chen, Yaming Hao, ..., Cheng Lian, Honglai Liu, Ming Gong

liancheng@ecust.edu.cn (C.L.)  
gongm@fudan.edu.cn (M.G.)

**Highlights**

Borate and fluoride create synergized neutral water oxidation for various catalysts

Hierarchical inner borate and outer fluoride anions enhance the water oxidation rate

Fluoride breaks the hydrogen bond network and pushes borate toward the interface

The interface structure enables low-cost and durable neutral water oxidation



Liu et al., Chem 8, 2700–2714  
October 13, 2022 © 2022 Elsevier Inc.  
<https://doi.org/10.1016/j.chempr.2022.06.012>



## Article

## Hierarchical anions at the electrode-electrolyte interface for synergized neutral water oxidation

Tao Liu,<sup>1,5</sup> Yuxin Chen,<sup>2,3,5</sup> Yaming Hao,<sup>1,5</sup> Jianxiang Wu,<sup>1</sup> Ran Wang,<sup>1</sup> Limin Gu,<sup>4</sup> Xuejing Yang,<sup>2</sup> Qiang Yang,<sup>2</sup> Cheng Lian,<sup>3,\*</sup> Honglai Liu,<sup>3</sup> and Ming Gong<sup>1,6,\*</sup>

## SUMMARY

The ion-enriched electrode-electrolyte interface is a unique characteristic of electrocatalytic reactions that can effectively tune the local chemical environment. In this study, we discovered a strong synergy between borate and fluoride anions for water oxidation in neutral conditions. Under an optimal ratio of the two anions, the water oxidation current significantly outperforms the individual counterparts by almost an order of magnitude. This synergy was greatly attributed to the hierarchical anions at the interface, with borate approaching the surface and fluoride extending out, as revealed by *in situ* surface-enhanced Raman spectroscopy and molecular dynamics simulation. This hierarchical anion arrangement created two kinetics regions, with one borate-dominating region to lower the onset potential and one fluoride-dominating region to sustain a larger current. Using the synergized electrolyte, a low-cost and facilely synthesized  $\text{Co}(\text{OH})_2$  electrode could achieve an outstanding performance of  $100 \text{ mA/cm}^2$  at  $1.791 \text{ V}$  versus RHE under  $\text{pH} = 7.87$  with a 2-week-long durability.

## INTRODUCTION

Oxygen evolution reaction (OER) is a key half reaction of electrochemical fuel or chemical production. It involves the simultaneous transfer of four electrons and four protons to the dioxygen formation, often with very sluggish kinetics that is limiting the overall efficiency of electrochemical transformation.<sup>1,2</sup> From mechanistic aspects, OER can be categorized into water oxidation in acidic or neutral conditions and hydroxide oxidation in highly alkaline conditions.<sup>3–5</sup> Among these categories, neutral water oxidation is the most challenging but highly desired in various applications, such as electrochemical  $\text{CO}_2$  reduction, seawater electrolysis, microbial electrolysis, and organic electrosynthesis.<sup>6–15</sup> The challenges lie in (1) the limited proton transfer rates for the proton-coupled electron transfer (PCET) involved in OER; (2) the limited catalyst choices of Ru-based, Ir-based, Co-based, Mn-based materials, etc. due to the local acidic environment accompanied by water oxidation; and (3) the restricted kinetics resulting from the polymeric water structures with strong hydrogen bonding as well as the dehydration process demanded for overcoming the strong ion-water interaction.<sup>16–29</sup>

In addition to the major efforts in the development of efficient electrocatalysts, engineering the electrode-electrolyte interface is a promising route toward enhancing the efficiency.<sup>30,31</sup> For instance, the Nocera group reported the Co-based catalyst and Ni-based catalyst in phosphate (P<sub>i</sub>) and borate (B<sub>i</sub>) electrolytes for greatly enhancing PCET events at the interface.<sup>32–34</sup> Li et al. and Shi et al. individually

## THE BIGGER PICTURE

The demand for carbon neutrality and sustainability has encouraged the development of electrochemical alternative processes with zero emission. However, current electrochemical transformations often need pH-extreme conditions, which significantly limit the applications demanding neutral conditions, such as  $\text{CO}_2$  electrolysis, microbial electrolysis, and organic electro-synthesis. The challenges lie in the inert polymeric water network and sluggish proton-coupled electron transfer rates in neutral media. In this research, we discovered a hierarchical anion structure at the electrode-electrolyte interface that enables efficient water oxidation with earth-abundant electrocatalysts. It extends beyond the current focus on catalyst development and emphasizes the significance of engineering the electrode-electrolyte interface, especially with hierarchical structures. It also opens up vast possibilities for electrochemical transformations in pH-benign conditions by this new interfacial structure.

discovered the promotion effect of surface-adsorbed chalcogenate and carboxylate on the OER activity via tuning the binding strength of oxygen intermediates.<sup>35,36</sup> Besides, Hunter et al. revealed the role of intercalated anion motifs for improving the catalytic activity of NiFe layered double hydroxide OER catalyst.<sup>37</sup> These efforts demonstrate the strong influence of local chemical environment on the kinetics of water oxidation. Despite that water is the dominating species near the electrode, the strongly adsorbing species as well as the surface-excess ions induced by the double-layer formation can disturb the surface water network for altering the water oxidation kinetics.

Here, we revealed a strong synergy between borate anions with acid-base reaction characteristics and fluoride anions with hydrogen-bonding characteristics to cooperatively facilitate the electrochemical water oxidation under neutral conditions with earth-abundant electrocatalysts. An optimized ratio of borate to fluoride could produce much larger currents compared with their individual counterparts. The electrochemical kinetics of the synergized system was studied in detail via Tafel analysis, H/D isotope exchange kinetics, and electrochemical impedance spectroscopy (EIS), showing two kinetics regions dominated by borate and fluoride, respectively. Furthermore, a combination of probe-assisted *in situ* surface-enhanced Raman spectroscopy (SERS) and molecular dynamics (MD) simulation revealed that this synergy is originated from the hierarchical anions at the electrode-electrolyte interface for activating water simultaneously. This synergized electrolyte could further enable high water oxidation activity and durability with a facilely accessible electrodeposited Co(OH)<sub>2</sub> electrode, holding great promise for future neutral water oxidation systems and electrochemical transformations.

## RESULTS

### Water oxidation needs activators: Borate, fluoride, and their synergy

Liquid water often exists in an inert polymeric network, creating grand obstacles for its activation and strongly relying on the alien species in water (Figures 1A and S1). We utilized a standard electrodeposited Co(OH)<sub>2</sub> electrode as the pre-catalyst electrode for our study. The electrode exhibited the morphology of flower-like stacking of nanoplates with the crystalline phase indexed to Co(OH)<sub>2</sub> (JCPDS 74–1057; Figure S2). In 0.5 M NaClO<sub>4</sub> without any other additives, the catalyst electrode showed very sluggish kinetics with emerging current only after 1.40 V versus the standard hydrogen electrode (SHE) (Figure S1A). This behavior was relatively independent of the pH, inconsistent with the catalytic PCET processes involved in water oxidation. A significant negative shift of the potential was observed at only pHs beyond 12, suggesting the more favorable oxidation of hydroxide anions (OH<sup>−</sup>) compared with H<sub>2</sub>O. Considering the proton gradient generated during water oxidation processes, we also analyzed the potential at only 0.3 mA/cm<sup>2</sup> to minimize the effect of local pH changes and exhibited similar trends (Figure S3A), further confirming the restricted kinetics of pure water oxidation possibly due to the inert polymeric water structures.

The addition of borate (B<sub>i</sub>) and fluoride could significantly facilitate the water oxidation but in a diverted manner. The introduction of borate anions created an onset current at ~1.05–1.10 V versus SHE but with a rapidly plateaued current afterward (Figures S1B and S3B), showing diffusion-limited behaviors. Increasing the borate concentrations only enhanced the plateaued current but did not shift the onset potential. The onset potential was also independent of pH, indicating the absence of free H<sup>+</sup> or OH<sup>−</sup> in the key elemental reactions. This phenomenon was attributed to the acid-base characteristics of borate anions for accepting the generated H<sup>+</sup>

<sup>1</sup>Department of Chemistry and Shanghai Key Laboratory of Molecular Catalysis and Innovative Materials, Fudan University, Shanghai 200438, China

<sup>2</sup>National Engineering Laboratory for Industrial Wastewater Treatment, East China University of Science and Technology, Shanghai 200237, China

<sup>3</sup>State Key Laboratory of Chemical Engineering, School of Chemistry and Molecular Engineering, East China University of Science and Technology, Shanghai 200237, China

<sup>4</sup>Trina Solar Co. Ltd, No. 2 Tianhe Road, Trina PV Industrial Park, Xinbei district, Changzhou 213031, Jiangsu, China

<sup>5</sup>These authors contributed equally

<sup>6</sup>Lead contact

\*Correspondence:  
liancheng@ecust.edu.cn (C.L.),  
gongm@fudan.edu.cn (M.G.)

<https://doi.org/10.1016/j.chempr.2022.06.012>

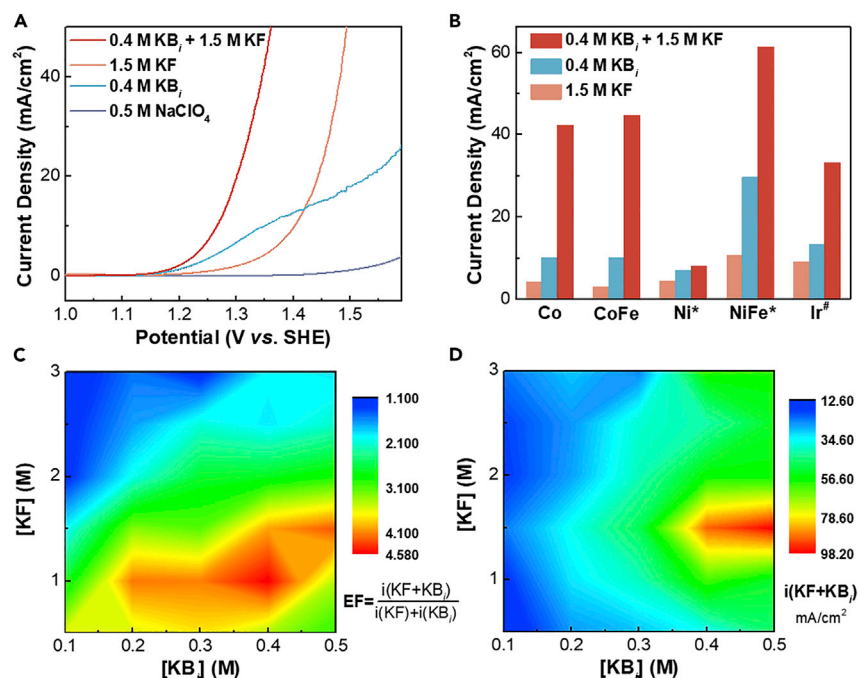


**Figure 1. Borate-fluoride synergized enhancement of neutral water oxidation**

(A) The comparison of LSV curves of the electrodeposited Co(OH)<sub>2</sub> electrode in 0.4 M KB<sub>i</sub> + 1.5 M KF, 0.4 M KB<sub>i</sub>, 1.5 M KF, and 0.5 M NaClO<sub>4</sub>.

(B) The summary of current densities on Co(OH)<sub>2</sub>, CoFe(OH)<sub>2</sub>, Ni(OH)<sub>2</sub>, NiFe(OH)<sub>2</sub>, and IrO<sub>x</sub> electrodes at 1.35 V versus SHE in 0.4 M KB<sub>i</sub> + 1.5 M KF, 0.4 M KB<sub>i</sub>, and 1.5 M KF. \*0.5 M KHCO<sub>3</sub> was added to ensure the stability of Ni-based electrocatalysts. #1.20 V versus SHE was used due to the relatively higher activity of the IrO<sub>x</sub> electrode.

(C and D) The heat diagrams of (C) the enhancement factors (defined as the current in 0.4 M KB<sub>i</sub> + 1.5 M KF divided by the numerical addition of the currents in 0.4 M KB<sub>i</sub> and 1.5 M KF) and (D) the absolute current densities under different combinations of KB<sub>i</sub> and KF concentrations.

from H<sub>2</sub>O, highly consistent with previous reports.<sup>32–34</sup> On the contrary, the addition of fluoride gradually shifted the curve toward more negative potentials without any plateaued current, implying a different pathway compared with borate (Figure S1C). Since the basic fluoride can induce pH changes at higher concentrations, we still observed the negative potential shift up to 2–3 M fluoride under the reversible hydrogen electrode (RHE) scale (Figure S3C), confirming the marked effect of fluoride for water activation. Fluoride is an excellent hydrogen-bond acceptor that can greatly disturb the polymeric hydrogen-bonding network in water, which may differ from the borate as H<sup>+</sup> acceptors for water activation. This hydrogen-bonding effect could be further evidenced by the red-shift of the O–D stretch in fluoride-containing D<sub>2</sub>O (Figure S4).

As borate and fluoride are activating water diversely, we envision that the simultaneous addition of borate and fluoride may synergize the water oxidation. Another impetus is the limitation of the high activity required for slightly alkaline borate and fluoride electrolytes while more neutral conditions are desired for practical applications. Excitingly, pairing borate and fluoride could significantly enhance the water oxidation activity at a neutral pH of 7.87 (Figure 1A). Compared with the KF electrolyte, the mixed KB<sub>i</sub>/KF electrolyte could negatively shift by ~140 mV, whereas compared with the KB<sub>i</sub> electrolyte, it could sustain a much higher current at larger overpotentials. At a potential of 1.40 V versus RHE, the current density in

the mixed electrolyte outperformed those in pure fluoride, pure borate, and their numerical addition by 9.49, 7.24, and 4.04 times, respectively. Such an effect could be generalized to various electrocatalysts, including CoFe hydroxide, Ni hydroxide, NiFe hydroxide, and Ir oxide, pointing to a general strategy of enhancing neutral water oxidation via borate-fluoride synergy (Figures 1B and S5). This synergy was further evaluated under different combinations of borate and fluoride concentrations (Figures 1C–1D and S6–S11). A larger enhancement factor (defined as the ratio of the current in the mixed electrolyte to the numerical addition of the currents in the individual counterparts at 1.40 V versus RHE) was present at lower fluoride concentrations but relatively less dependent on the borate concentration. Meanwhile, the absolute current density is higher under larger borate concentrations and shows a volcano-like dependence on fluoride concentrations with a maximal value at 1.5 M fluoride. Under the optimal electrolyte composition of 0.4 M  $\text{KB}_i$  and 1.5 M KF, both significant synergy and high current density could be achieved. This dependence is likely derived from the stronger affinity of borates to the oxide/hydroxide-based catalyst surface than the fluorides. At larger fluoride concentrations, the borates could be easily substituted by fluoride due to the huge concentration discrepancy, thus causing the loss of synergy. The activity dependence was further confirmed by evaluating the activities on the electrodeposited  $\text{Co}(\text{OH})_2$  on a planar rotating disk electrode (RDE) at 1,000 rpm (Figures S12–S18). Similar trends of borate-fluoride synergy could be derived, but higher enhancement factors could be derived at lower borate concentrations on RDE electrodes, presumably due to the low-surface-area planar electrodes that demand sufficiently less borate to cover the electrode and thus enhance the water oxidation activity in low-concentration borate electrolytes. Nevertheless, the highest activity could still be obtained in 0.4 M  $\text{KB}_i$  and 1.5 M KF and, therefore, was utilized as the standard condition for the later study.

### Electrochemical kinetics under borate/fluoride synergy

To glean the underlying mechanism of the borate/fluoride synergy, we first excluded the possible structural changes induced by the electrolytes. Anodizing  $\text{Co}(\text{OH})_2$  in various electrolytes led to only slight changes in the water oxidation activities in bare 0.5 M  $\text{NaClO}_4$  electrolyte, demonstrating a primary electrolyte effect for the activity enhancement. The anodized catalyst exhibited the enhancement of the lattice  $\text{O}^{2-}$  X-ray photoelectron spectroscopy (XPS) signal as well as the relative  $\text{Co}^{3+}$  ratio, corresponding to the evolution of the  $\text{CoOOH}$  phase via electrochemical oxidation (Figure S19). This was consistent with previous literature reports of the XPS changes after anodization.<sup>38</sup> Trace amounts of F and B XPS signals were also detected for the anodized catalyst, possibly due to the irreversible adsorption or anion intercalation (Figures S19E and S19F). However, these slight structural changes could barely affect the water oxidation activity via exhibiting similar activity trends for the anodized catalyst, confirming the critical borate/fluoride synergy at the electrode-electrolyte interface (Figure S20). The possible contribution of Fe impurities in the electrolyte was also excluded with almost identical activities in un-purified and purified electrolytes (Figure S21).

We then compared the electrochemical kinetics via the Tafel analysis (Figure 2A). In 1.5 M KF, the Tafel slope was calculated to be  $\sim 133$  mV/decade, which is close to the theoretical value of 120 mV/decade for the rate-limiting first electron transfer step, whereas in 0.4 M  $\text{KB}_i$ , a Tafel slope of 81.8 mV/decade was obtained at lower overpotentials, which reflects a faster electron transfer, but the current quickly plateaued with a very short Tafel region, possibly due to the inhibitory effect of borate on the surface.<sup>33</sup> In the synergized 0.4 M  $\text{KB}_i$  + 1.5 M KF electrolyte, the kinetics

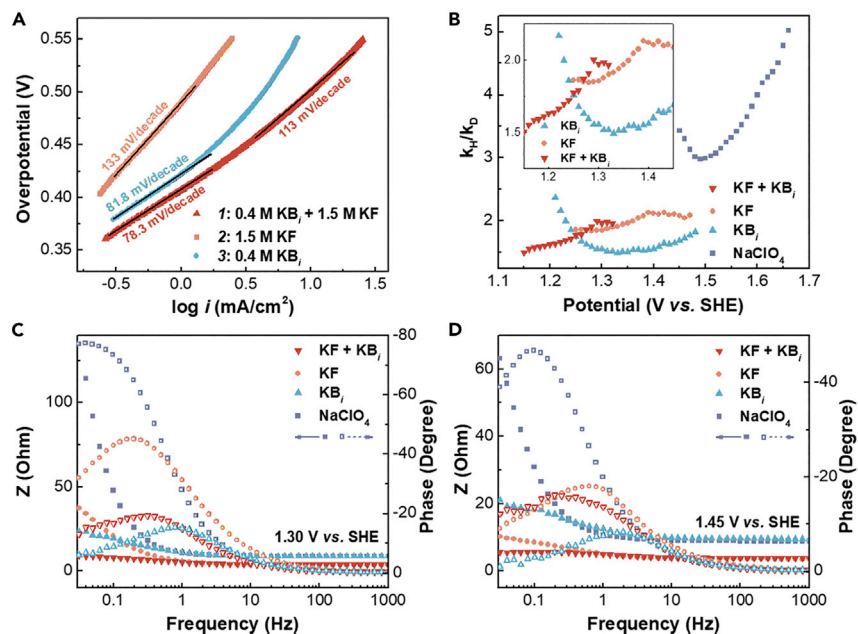


**Figure 2. Electrochemical kinetics of the borate-fluoride synergy**

(A) The Tafel plots in 0.4 M  $\text{KB}_3$  + 1.5 M KF, 0.4 M  $\text{KB}_3$ , and 1.5 M KF electrolytes.

(B) The kinetic isotope effect (KIE) values at different potentials in 0.5 M  $\text{NaClO}_4$ , 0.4 M  $\text{KB}_3$  + 1.5 M KF, 0.4 M  $\text{KB}_3$ , and 1.5 M KF electrolytes.

(C and D) The Bode plots in 0.5 M  $\text{NaClO}_4$ , 0.4 M  $\text{KB}_3$  + 1.5 M KF, 0.4 M  $\text{KB}_3$ , and 1.5 M KF electrolytes at (C) 1.30 V versus SHE and (D) 1.45 V versus SHE.

demonstrated two Tafel regions with  $\sim 78.3$  mV/decade at relatively lower overpotentials close to the  $\text{KB}_3$  kinetics and  $\sim 113$  mV/decade at higher overpotentials close to the KF kinetics, showing the dominating effects of each anion in different kinetic regions. It is worth noting that in spite of the similar Tafel slopes at larger overpotentials (mixed versus KF), the current density is larger by almost one order of magnitude, which sets up the foundation for the synergy. The similar Tafel slopes with larger current densities clearly indicate the significantly enhanced exchange current density. It is probably derived from the altered  $\text{H}_2\text{O}$  chemical environment under quasi-equilibrium conditions, likely due to the borate anions in the vicinity of the electrode. Moreover, we carried out the H/D kinetic isotope effect (KIE) experiments to investigate the H-involved kinetics in borate/fluoride synergy (Figure 2B). In 0.5 M  $\text{NaClO}_4$ , the  $k_{\text{H}}/k_{\text{D}}$  ratios reached  $>3$  with increasing values at higher overpotentials, indicating a primary KIE due to the strong hydrogen-bonding water network. The facilitated  $\text{H}_2\text{O}$  activation showed smaller KIE values. In 0.4 M  $\text{KB}_3$ , the average KIE value lies in 1.50–1.60, whereas in 1.5 M KF, the KIE value gradually increases from 1.86 (low overpotential) to  $\sim 2.10$  (high overpotential) and then plateaus. The different KIEs in fluoride and borate systems further corroborated their different activation mechanism. The mixed borate/fluoride electrolyte demonstrated a similar trend of increasing and then plateaued KIE value as the KF electrolyte, but the value is 0.1–0.3 lower than KF, approaching the  $\text{KB}_3$  electrolyte. These phenomena point to a general synergy mechanism of borate-dominating activation at low overpotentials and fluoride-dominating activation at high overpotentials with significantly enhanced exchange current density via the act of borate to modulate the water environment.

The borate-fluoride synergy likely arises from the interfacial properties at the electrode-electrolyte interface. Accordingly, we carried out EIS analysis under different

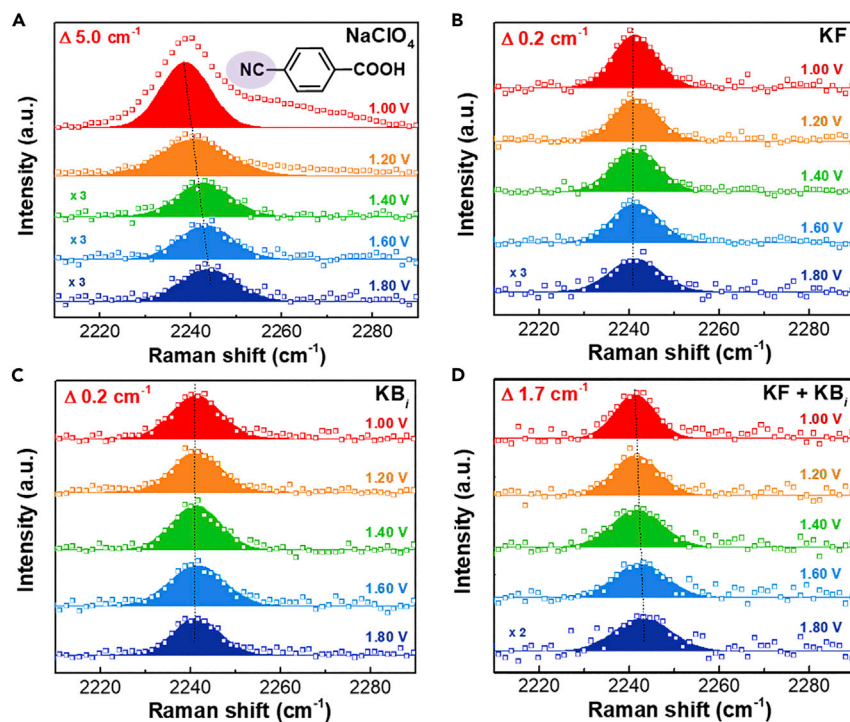


**Figure 3. Probe-assisted *in situ* SERS of the local interfacial structure**

(A–D) The *in situ* SERS spectra of the 4-cyanobenzoic acid (10 mM) on the roughened gold electrode in different electrolytes under different applied potentials.

applied potentials. Under a relatively low overpotential of 1.30 V versus SHE, we could observe a higher resemblance of the phase diagram of the Bode plot for the mixed borate/fluoride electrolyte to the borate electrolyte than to the fluoride electrolyte, suggesting the interfacial property mostly governed by the surface-enriched borate anions. However, when the potential was increased to 1.45 versus SHE, we observed the trend of the mixed electrolyte aberrating from the  $\text{KB}_3$  electrolyte and approaching the KF electrolyte in the phase diagram (Figures 2C and 2D), confirming the aforementioned two kinetic regions and the borate/fluoride synergy. Importantly, the total impedance was significantly reduced in the mixed electrolyte, especially for the charge-transfer resistance (Figures 2C, 2D, and S22), which corroborates the much faster electron transfer under the synergy. The accelerated electron transfer could further induce pH-dependent kinetics in a wide pH range of 7–12 in the mixed electrolyte (Figure S23). The potential shift per pH was fitted to be  $\sim 60.94$  mV/pH, close to the Nernst shift for the PCET step involving  $1 \text{ H}^+$  per  $\text{e}^-$ . It is worthwhile to note again that in the absence of any water activator, the water oxidation kinetics is relatively independent of pH before the emergence of  $\text{OH}^-$  oxidation, and the synergy of borate and fluoride activators could significantly facilitate the interfacial charge transfer toward PCET-type kinetics typically with lower energy barriers.

#### ***In situ* surface-enhanced Raman spectroscopy for probing anion distribution**

We further carried out *in situ* SERS to investigate the borate/fluoride synergy at the electrode-electrolyte interface (Figure 3). We attempted to compare the SERS spectra of the interfacial water on roughened gold electrode under different electrolytes. In the mixed borate/fluoride electrolyte, slightly enhanced symmetric bending bands ( $\nu_{2a_1}$ ) at  $3,253 \text{ cm}^{-1}$  and asymmetric stretching bands ( $\nu_{3b_1}$ ) at  $3,452 \text{ cm}^{-1}$

relative to the symmetric stretching bands ( $\nu_3b_1$ ) at  $3,606\text{ cm}^{-1}$  upon deconvolution were observed at higher applied potentials (Figure S24). However, the limited signal enhancement on gold at anodic potentials and the presence of a huge bulk water signal near the electrode-electrolyte interface could bury the interfacial water signal, causing significant difficulty in identifying the synergistic effect of anions on the water structure. Consequently, we utilized a dynamically adsorbing probe of 4-cyanobenzoic acid to reflect the interfacial effect. Under anodic potentials, the carboxylate moieties can reversibly adsorb and desorb on the gold electrode, whereas the cyano tag can be enhanced for probing the interface. The Stoke's shift of the cyano group has been known to be indicative of the local electric field and chemical environment.<sup>39</sup> In bare  $\text{NaClO}_4$  electrolyte, the  $-\text{CN}$  Raman band gradually blue shifted from  $2,038.7$  to  $2,043.7\text{ cm}^{-1}$  (the change in the Raman shift  $\Delta = 5.0\text{ cm}^{-1}$ ) upon increasing applied potentials, consistent with the previous observation at more negative potentials<sup>39,40</sup> (Figure 3A). However, the Raman band remained unchanged at  $2,241.3\text{ cm}^{-1}$  with a shift range within  $0.2\text{ cm}^{-1}$  in  $\text{KB}_i$  or  $\text{KF}$  electrolytes alone independently of the applied potentials (Figures 3B and 3C). The absence of the peak shift resulted from the incapability of penetrating the electrical double layer for the cyano probes, which likely stemmed from the large concentration disparity ( $10\text{ mM}$  versus  $0.4$  or  $1.5\text{ M}$ ) as well as the high affinity of borate and fluoride anions to the electrode under anodic potentials. Therefore, the measured Raman band was only indicative of the probes residing in the outer Helmholtz layer or the diffusion layer, not much different from the bulk counterpart. Nevertheless, in the mixed electrolyte, the shift in Raman bands was partially restored with a total shift of  $1.7\text{ cm}^{-1}$  ( $\Delta = 1.7\text{ cm}^{-1}$ , Figure 3D). Although this shift was rather insignificant compared with the  $\text{NaClO}_4$  case, it was much higher than the individual counterparts. Theoretically, the presence of both borate and fluoride anions should block the probe to a greater extent, causing negligible band position shifts. The shift was clearly indicative of the local structural change in the mixed borate/fluoride electrolytes. There are two possibilities causing this phenomenon: (1) the construction of a local electrode-electrolyte interface that significantly differs from the individual counterparts, stabilizing the cyano probe near the electrode, and (2) the mixed electrolyte creates a stronger electric field locally to influence the Raman shift of the cyano probe. The two possibilities both illustrate the different interfacial anion structures compared with the single anions, which is likely the cause of borate/fluoride synergy.

In addition to the probe-assisted *in situ* SERS study, we also electrodeposited  $\text{Co}(\text{OH})_2$  on the gold electrode to compare its structural evolution under different electrolytes (Figure S25). The large broad peak centered at  $574\text{ cm}^{-1}$  under  $1.10\text{ V}$  versus SHE in borate or fluoride electrolyte is often attributed to the gold oxide formed under anodic potentials.<sup>41</sup> Increasing the potential beyond  $1.40\text{ V}$  versus SHE evolved two major peaks at  $586\text{ cm}^{-1}$  and  $630\text{ cm}^{-1}$ , possibly related to the Co species involving amorphous  $\text{CoO}_x$  or  $\text{CoOOH}$  (Figure S25A).<sup>42</sup> In the  $\text{KB}_i$ ,  $\text{KF}$ , or the mixed electrolytes, the spectra all exhibited the evolution of a large broad peak centered at  $\sim 585\text{--}587\text{ cm}^{-1}$  with two shoulder peaks on each side, suggesting the evolution of similar bulk Co species in these electrolytes (Figures S25B and S25C). It points to a smaller effect of electrolyte anions on the bulk catalyst structure, but instead an influence on the electrode-electrolyte interface. By further comparing the detailed difference spectra between  $1.20$  and  $1.60\text{ V}$ , we observed a slightly larger resemblance of the mixed electrolyte to the  $\text{KB}_i$  electrolyte, whereas the  $\text{KF}$  electrolyte showed a more blue-shifted peak (Figure S26), possibly indicating that the surface property is more influenced by the borate with a higher affinity of borate to the surface. This was further evidenced

by the more obvious Co redox peaks in the cyclic voltammetry (CV) curves of the electrolytes in pure  $\text{KB}_i$  and mixed  $\text{KB}_i/\text{KF}$  electrolytes (Figure S27).

### Hierarchical borate/fluoride anions in the more compact double layer

Another interesting phenomenon observed is the distinct behaviors under different  $\text{KB}_i/\text{KF}$  addition orders (Figure S28). We utilized the single component electrolyte to first stabilize the electrical double layer and then introduced the second component for recording the current changes. In both cases, the addition of the second component induced drastic increases in the current densities according to the borate/fluoride synergy. However, the addition of borate to the fluoride electrolyte exhibited a steady current increase followed by a stabilized current afterward, whereas the addition of fluoride to the borate electrolyte demonstrated a rapid current increase followed by a steady decrease toward an eventually stabilized current. This phenomenon was further supported by the rapid-scanning CVs under different borate/fluoride orders (Figure S29). We envisioned that such behaviors could be caused by the local borate/fluoride structures and different anion rearrangement events during the different addition orders. Therefore, we further performed MD simulation to analyze the distribution of the anions and water molecules near the catalyst surface under different systems and different applied potentials (Figures 4, S30, and S31; Tables S1 and S2). In pure borate or pure fluoride systems, the anions are located at least 5 Å away from the electrode surface, whereas with borate/fluoride synergy, the borate is pushed closer to the surface within 3 Å for the first distribution peak (Figure 4B). Comparatively, the fluoride remains at the same position as the pure electrolyte, further away from the surface. This depicts a hierarchical anion structure in the electrical double layer with borate at the inner layer and fluoride at the outer layer. The presence of fluoride on the outer spheres induces a more compact borate inner layer, which is likely resulted from the breaking of the aqueous hydrogen-bonding network. The more compact double layer was also evidenced by the larger capacitance derived from CVs and charge integration from the pulse amperometry (Figure S32). Moreover, under different applied potentials, the borate remains relatively unchanged in its allocation, whereas the fluoride gradually moves closer to the electrode surface with increasing potentials (Figures 4C and 4D). The higher fluoride concentration near the vicinity of the electrode can be a great contributor to the sustainment of higher current under larger overpotentials. These MD simulation results well supported the kinetics and *in situ* SERS measurement for creating the hierarchical structure of the compact borate layer that lowers the overpotential and outer fluoride layer with more compact structures at larger overpotentials to sustain the large current.

We also simulated the local anion distribution in the double layer upon different addition orders (Figure S33). The addition of fluoride to borate immediately pushed some of the borate anions toward the inner layer, whereas the added fluoride anions tend to reside slightly further away from the electrode. This was probably due to the breaking of the hydrogen-bonding network by the added fluoride anions, but in the meantime, it possibly required more time to stabilize the local structures via the rearrangement of anions for re-generating the hydrogen-bonding network. Reverting the addition order of borate to fluoride exhibited a lag in the borate re-distribution with borate mostly residing on the outer peripherals of the double layer. This might be attributed to the enriched fluoride anions in the same region with a disconnected hydrogen-bond network. Upon the applied potentials, the borate anions could gradually approach the electrode surface without disturbing the fluoride distribution too much. Therefore, we obviously derived different anion rearrangement behaviors upon different addition orders with the fluoride addition affecting both fluoride and

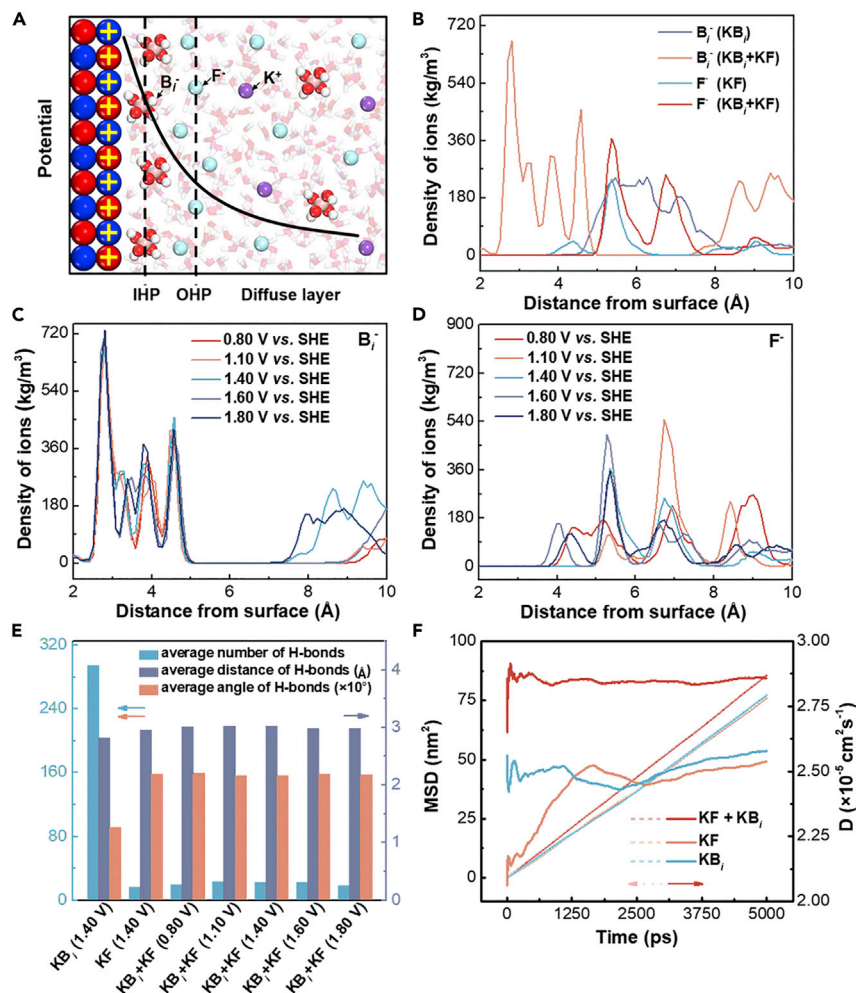


**Figure 4. MD simulation of the borate-fluoride interfacial layer**

(A) Schematic diagram of anion distribution in the electric double layer.

(B) The radial distribution of  $B_i^-$  and  $F^-$  anions in different systems.

(C and D) The radial distribution of (C)  $B_i^-$  and (D)  $F^-$  anions in the mixed system under different applied potentials.

(E) The statistical results of the hydrogen bonds under different systems and different applied potentials.

(F) The MSD and self-diffusion coefficient of water molecules in the electric double layers of different systems.

borate distribution and the borate addition only affecting its own distribution, which might explain the distinct behaviors of the addition-order experiment.

Based on the optimized structure of the anions in the electrical double layer, we further analyzed the properties of water in these systems, as water is the OER reactant (Figures 4, S34, and S35). The results reflect that the fluoride anions can greatly disturb the hydrogen-bonding network with decreasing number of hydrogen bonds between water molecules as well as the increasing average angles of the hydrogen bonds compared with the borate system (Figure 4E). This largely resulted from the high affinity of fluoride anions with water to form intermolecular hydrogen bonds. The hydrogen bond properties in the borate/fluoride system highly resemble the pure fluoride system (Figure 4E), demonstrating the central role of fluoride anions in governing the hydrogen bonds. The disturbed water hydrogen-bonding network

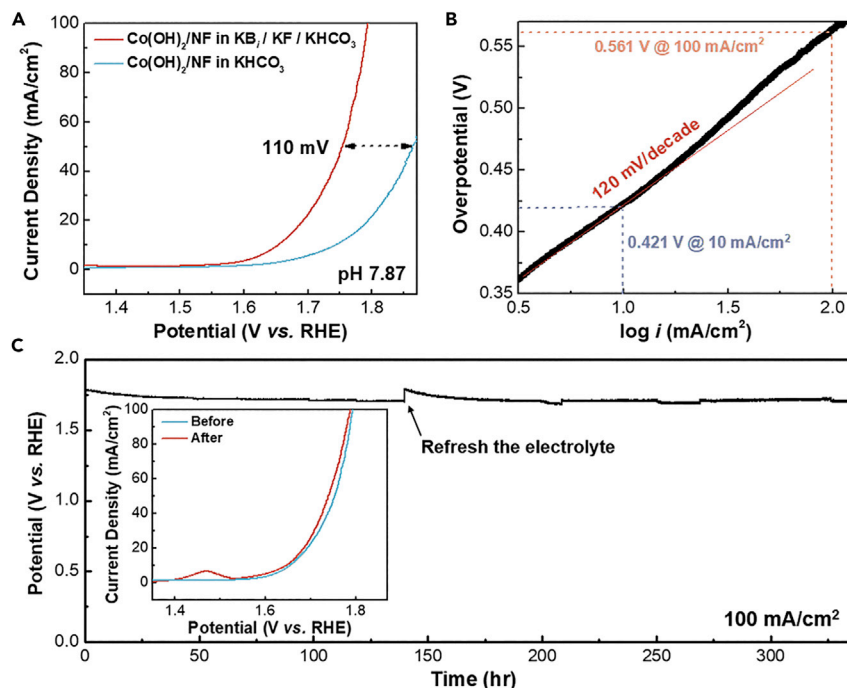


**Figure 5. High-performance neutral water oxidation under borate-fluoride synergy**

(A) The LSV curves of Co(OH)<sub>2</sub> pre-catalyst on Ni foam in 0.5 M KHCO<sub>3</sub> and 0.5 M KHCO<sub>3</sub> + 0.4 M KB<sub>1</sub> + 1.5 M KF.

(B) The Tafel plot of Co(OH)<sub>2</sub> pre-catalyst on Ni foam in 0.1 M KHCO<sub>3</sub> + 0.4 M KB<sub>1</sub> + 1.5 M KF.

(C) The long-term stability of Co(OH)<sub>2</sub> pre-catalyst on Ni foam in 0.5 M KHCO<sub>3</sub> + 0.4 M KB<sub>1</sub> + 1.5 M KF at a constant current density of 100 mA/cm<sup>2</sup>. The inset shows the LSV curves before and after the stability test.

by the fluorides may create more open space for the borate to penetrate deeper into the interface. In addition, the bulk hydrogen bond properties are mostly maintained under different potentials, implying that the bulk hydrogen bond in the electrolyte is not a key factor for current changes upon applied potential. Another interesting finding is that the mean square displacement (MSD) and self-diffusion coefficient of water molecules are larger in the mixed borate/fluoride system compared with the individual pure electrolytes. In spite of the similarly disturbed hydrogen bonds in mixed fluoride/borate and pure fluoride systems, the larger self-diffusion coefficient of water indicates more active water molecules induced by the presence of borate anions. The self-diffusion coefficient is often governed by temperature and local electric field, and since the temperature is fixed in our simulation, we speculate that the larger self-diffusion is likely contributed by the larger local electric field felt by the water molecules, which is consistent with our hypothesis from the cyano-probe assisted Raman spectroscopy study and is further evidenced by large charge perturbations at the electrode-electrolyte interface for the mixed electrolyte via simulation (Figure S36). This electric field enhancement could be stemmed from the more compact double layer and the hierarchical anion distribution at the electrode-electrolyte interface, which points to a new direction of optimizing the catalytic activity for electrochemical reactions.

#### Applications of the synergized electrolyte for water oxidation in CO<sub>2</sub>-reduction electrolytes

The borate/fluoride synergy further encourages the application in neutral water oxidation scenarios. One highly relevant scenario is the CO<sub>2</sub> electrolysis in neutral

conditions, and therefore, we added 0.5 M potassium bicarbonate ( $\text{KHCO}_3$ ) to our optimized borate/fluoride electrolyte and studied the catalytic performance of the  $\text{Co}(\text{OH})_2$ -based electrode (Figure 5). The  $\text{Co}(\text{OH})_2$  catalyst was electrodeposited onto a porous Ni foam with high loadings to maximize the catalytic activity. The  $\text{Co}(\text{OH})_2/\text{Ni}$  foam electrode could achieve a potential gain of 110 mV in the mixed borate/fluoride electrolyte compared with the bare  $\text{KHCO}_3$  electrolyte, as well as the current densities of 10 and 100  $\text{mA}/\text{cm}^2$  at 1.651 and 1.791 V versus RHE, respectively. The electrode could sustain the Tafel regions within a large current density span without showing much diffusion-limited kinetics that is often typical of neutral water oxidation (Figure 5B). This performance is among the highest activities for neutral OER using earth-abundant electrocatalysts, approaching the precious-metal-based electrocatalysts (Table S3). Besides the higher efficiency, the catalyst electrode could constantly sustain 100  $\text{mA}/\text{cm}^2$  at 1.70–1.75 V for 2 weeks (336 h) without much activity decay (Figure 5C). The linear sweep voltammetry (LSV) after the stability exhibited no activity decay, only with partial oxidation of the Ni foam surface under long-term anodization. This demonstrates a high promise of this mixed borate/fluoride electrolyte for real electrolytic applications of neutral water oxidation, such as  $\text{CO}_2$  electroreduction. Although borate and fluoride anions mostly accumulated on the anode upon applied potentials, the high anion concentrations and possible irreversible adsorption might influence the cathodic reactions, such as  $\text{CO}_2$  electroreduction, which desires further detailed study for future two-electrode real applications.

## DISCUSSION

In this report, we discovered the synergistic effect of hierarchical anions, borate and fluoride, for cooperatively promoting electrocatalytic water oxidation in neutral conditions. Under anodic potentials, borate anions tend to reside in the inner Helmholtz layer closer to the catalyst surface, whereas fluoride anions are located further outside. More anodic potentials do not alter the arrangement of the ions but gradually move the fluoride anions toward the electrode-electrolyte interface. The hierarchical anions could greatly enhance the electrocatalytic activity of water oxidation, especially on an electrodeposited  $\text{Co}(\text{OH})_2$  electrode. The current outperforms the individual counterpart as well as the numerical addition by 9.49, 7.24, and 4.04 times at 1.40 V versus RHE. This synergy could lead to two kinetic regions: one is the borate-dominating region that facilitates the water oxidation onset by encouraging local PCET events and the other is the fluoride-dominating region facilitated by borate anions that sustain higher current via greatly enhancing the exchange current density. These findings were revealed by a combinatory approach of electrochemical kinetics, H/D exchange kinetics, EIS, and *in situ* SERS. This synergized electrolyte could eventually enable highly effective water oxidation in neutral pHs to simultaneously achieve high current densities of 10 and 100  $\text{mA}/\text{cm}^2$  at 1.651 and 1.791 V versus RHE and great durability of  $\sim 336$  h at 100  $\text{mA}/\text{cm}^2$ , opening new possibilities for efficient electrolytic applications in neutral conditions.

## EXPERIMENTAL PROCEDURES

### Resource availability

#### Lead contact

Further information and requests for resources and reagents should be directed to and will be fulfilled by the lead contact, Ming Gong (gongm@fudan.edu.cn).

#### Materials availability

This study did not generate new unique reagents.

### Data and code availability

There is no dataset or code associated with this paper.

### Chemicals

All reagents were used as received without further purification. Cobalt nitrate hexahydrate ( $\text{Co}(\text{NO}_3)_2 \cdot 6\text{H}_2\text{O}$ , 99%), manganese(II) nitrate tetrahydrate ( $\text{Mn}(\text{NO}_3)_2 \cdot 4\text{H}_2\text{O}$ , 98%), nickel(II) nitrate hexahydrate ( $\text{Ni}(\text{NO}_3)_2 \cdot 6\text{H}_2\text{O}$ , 99%), iron(III) nitrate nonahydrate ( $\text{Fe}(\text{NO}_3)_3 \cdot 9\text{H}_2\text{O}$ , 98%), iridium chloride hydrate ( $\text{IrCl}_3 \cdot x\text{H}_2\text{O}$ , 99.9%), oxalic acid dihydrate ( $\text{C}_2\text{H}_2\text{O}_4 \cdot 2\text{H}_2\text{O}$ , 99.8%), sodium carbonate anhydrous ( $\text{Na}_2\text{CO}_3$ , AR), potassium fluoride anhydrous (KF, 99.0%), boric acid ( $\text{H}_3\text{BO}_3$ , 99.5%), sodium perchlorate ( $\text{NaClO}_4$ , 99.0%), potassium bicarbonate ( $\text{KHCO}_3$ , AR), deuterium oxide (98 atom % D,  $\text{D}_2\text{O}$ ), ethanol ( $\geq 99.7\%$ ), and 4-cyanobenzoic acid (98.0%) were purchased from Aladdin Industrial Corporation (China). The perchloric acid ( $\text{HClO}_4$ , 70.0%–72.0%) was obtained from Shanghai Titan Scientific (China). The sulfuric acid ( $\text{H}_2\text{SO}_4$ , 95.0%–98.0%) and potassium hydroxide (KOH,  $\geq 85$  wt %) were purchased from Sinopharm Chemical Reagent (China). The carbon fiber paper (CFP) was purchased from Hesen Electric (HCP020N, China). The nickel foam was purchased from Guangjiayuan New Material. The ultrapure deionized water ( $18.2 \text{ M}\Omega \cdot \text{cm}^{-1}$ ,  $25^\circ\text{C}$ ) was purified by the ELGA purification system (China).

### Catalyst electrode preparation

The Co-based, Ni-based, Mn-based, and Ir-based catalysts were first electrodeposited on the CFP in a three-electrode H-type electrochemical cell with the Ag/AgCl electrode as the reference electrode. The CFP was tailored to the size of  $1 \times 2 \text{ cm}^2$  with the active area of  $1 \text{ cm}^2$  as both the working electrode and counter electrode. All electrolytes for the electrodeposition process are described in the electrolyte preparation part. The  $\text{Co}(\text{OH})_2$  catalyst was obtained by applying a cathodic current density of  $5 \text{ mA/cm}^2$  for 60 s in 0.1 M  $\text{Co}(\text{NO}_3)_2$ . The  $\text{CoFe}(\text{OH})_2$ ,  $\text{Ni}(\text{OH})_2$ , and  $\text{NiFe}(\text{OH})_2$  catalysts were obtained by the identical procedure (with 5 atom % Fe relative to Co or Ni). The Mn-based catalyst was obtained by applying the same current density for 5 min. The Ir-based catalyst was prepared by applying 0.8 V for 10 min. The Co-based catalyst electrodeposited on the CFP was used after being washed by ethanol and ultrapure deionized water and dried in a vacuum oven at  $60^\circ\text{C}$ , and the Mn-based and Ir-based catalysts were further sintered for 1 h under  $300^\circ\text{C}$ . The Co-based catalyst on the nickel foam were obtained by a similar procedure with the extension of the electrodeposition duration to 30 min.

### Electrolyte preparation

(1) Electrodeposition electrolyte: 5 mmol  $\text{Co}(\text{NO}_3)_2 \cdot 6\text{H}_2\text{O}$  or 5 mmol  $\text{Ni}(\text{NO}_3)_2 \cdot 6\text{H}_2\text{O}$  or 5 mmol  $\text{Mn}(\text{NO}_3)_2 \cdot 4\text{H}_2\text{O}$  were dissolved in 50 mL deionized water for electrodeposition of Co-based, Ni-based, and Mn-based catalyst, respectively. For Fe-doped catalysts, 0.5 mmol  $\text{Fe}(\text{NO}_3)_3 \cdot 9\text{H}_2\text{O}$  was added to the electrolyte. For the Ir-electrodeposition electrolyte, 20 mM  $\text{IrCl}_3 \cdot x\text{H}_2\text{O}$  was added into 50 mL deionized water and constantly stirred until complete dissolution, then 50 mg  $\text{C}_2\text{H}_2\text{O}_4 \cdot 2\text{H}_2\text{O}$  was slowly added to coordinate to the  $\text{IrCl}_3$ , and finally,  $\text{Na}_2\text{CO}_3$  was utilized to regulate the pH to 10.50. (2) Electrolyte for electrochemical measurement: (1) pH = 0–14 solution:  $\text{HClO}_4$  and KOH were used to adjust the pH to values varying from 0 to 14 with the deviation  $\leq 0.02$ ; (2)  $\text{NaClO}_4$  electrolyte: 25 mM  $\text{NaClO}_4$  was added into 50 mL deionized water, and then, the pH was changed to 7.87; and (3)  $\text{KB}_i$ , KF, and mixed electrolytes: different concentrations of  $\text{H}_3\text{BO}_3$  and KF were added to the deionized water, and the pH was adjusted by adding  $\text{HClO}_4$  and KOH.

### Electrochemical studies

The electrochemical measurements were carried out on a CHI 660E potentiostat (Shanghai Chenhua Instruments) using a graphite rod, Ag/AgCl electrode, and as-prepared catalyst electrode as the counter electrode, the reference electrode, and the working electrode, respectively, in a standard 100 mL H-type electrochemical cell. The RDE (AMETEK Model 636A) was used as the working electrode with a rotating rate of 1,000 rpm. Before testing, CV measurement was conducted to activate the electrode and stabilize it by equilibrating with air under a scan rate of 100 mV/s from 0.4 to 1.0 V for 5 cycles. LSV was conducted at a scan rate of 1 mV/s to study the kinetics. The stability test was carried out under the constant current density of 100 mA/cm<sup>2</sup> using the Co-based catalyst on the nickel foam. All experiments were implemented at room temperature. The measured potentials were referenced to the SHE using the equation of  $E(\text{SHE}) = E(\text{Ag}/\text{AgCl}) + 0.197 \text{ V}$ . Some potentials were converted to the RHE scale by further addition of  $0.0591 \times \text{pH}$ . All LSV curves were iR-compensated for consistent comparison. The EIS measurement was conducted on the Gamry INTERFACE 1010E under the applied potentials of 0.90–1.60 V versus Ag/AgCl with the frequency ranging from 0.01 to 10,000 Hz. The H/D exchange experiment was carried out under almost identical conditions except that a 10 mL H-type electrochemical cell was utilized for minimizing the use of D<sub>2</sub>O. All pHs were calibrated by a pH meter (PHSJ-3F, INESA Scientific Instrument, China).

### Materials and spectroscopic characterization

The as-prepared Co-based catalyst on CFP was utilized for characterization. The X-ray diffraction (XRD) was obtained on a D2 PHASER with 5–90°. The scanning electron microscopy (SEM) images were recorded by Zeiss Sigma300 with an accelerating voltage of 10 kV. The XPS was obtained on Thermo Scientific K-Alpha and the C 1s binding energy at 284.8 eV was used for calibration. The inductively coupled plasma-mass spectrometry (ICP-MS) was conducted on the Agilent 7700. The Raman spectra were recorded using a 2,400/mm grating by Raman spectrometer (Horiba Jobin Yvon) with a 638 nm laser. The resolution and the acquisition time are set to about 1.3 cm<sup>-1</sup> and 20 s, respectively. The customized three-electrode cell (EC-RAIR, Beijing Science Star Technology) was used for the *in situ* Raman spectroscopy measurement, using the Pt wire, the Ag/AgCl electrode, and a roughened gold surface as the counter electrode, the reference electrode, and the working electrode. The modified Co-based catalyst on the roughened gold substrate was prepared by the almost identical electrodeposition conditions except for the current density of 1 mA/cm<sup>2</sup> and the deposition time of 30 s. 10 mM of the probe molecule (4-cyanobenzoic acid) was directly added to the electrolyte during electrolyte preparation.

### Molecular dynamics simulation

A potential difference of 0.8–1.8 V was applied to the two oxide electrodes (to mimic the catalyst surface), and MD simulation was carried out at a constant potential. We chose CHARMM 36 force field for modeling and simulation, which has good support for many elements. According to the concentration of borate and fluoride, 37 fluorine ions, 10 borate ions, 47 potassium ions, and 1,220 water molecules were added to the system (the weights of various molecules in the single anion systems are different). The OPC model was adopted for water molecules, which can accurately reflect various properties of water. Energy minimization was carried out before the MD simulation to ensure the rationality of the initial configuration and improve the efficiency and reliability of the calculation. The formal simulation adopts an NVT ensemble, takes 1 fs as step size, carries out 40 ns simulation, and outputs one frame

every 1 ps. During the analysis, 10,000 frames were extracted in steps of 1 ps in the last 10 ns trajectory to eliminate accidental errors.

### SUPPLEMENTAL INFORMATION

Supplemental information can be found online at <https://doi.org/10.1016/j.chempr.2022.06.012>.

### ACKNOWLEDGMENTS

M. Gong acknowledges the support from the Shanghai Technology Innovation Program (Carbon-Neutral Program, 21DZ1207800), the National Key R&D Program of China (2019YFC1604602), and the National Natural Science Foundation of China (22172036). C.L. acknowledges the support from the National Natural Science Foundation of China (22078088).

### AUTHOR CONTRIBUTIONS

T.L. and M.G. conceived the project. T.L. and Y.H. conducted the experimental work. Y.C. and C.L. carried out the molecular dynamics simulation. T.L., Y.C., Y.H., J.W., R.W., L.G., X.Y., Q.Y., C.L., H.L., and M.G analyzed the data. T.L, Y.C., Y.H., C.L., and M.G. co-wrote the manuscript.

### DECLARATION OF INTERESTS

The authors declare no competing interests.

Received: December 27, 2021

Revised: February 8, 2022

Accepted: June 15, 2022

Published: July 15, 2022

### REFERENCES

1. Song, J.J., Wei, C., Huang, Z.F., Liu, C.T., Zeng, L., Wang, X., and Xu, Z.J. (2020). A review on fundamentals for designing oxygen evolution electrocatalysts. *Chem. Soc. Rev.* 49, 2196–2214. <https://doi.org/10.1039/c9cs00607a>.
2. Gao, L.K., Cui, X., Sewell, C.D., Li, J., and Lin, Z.Q. (2021). Recent advances in activating surface reconstruction for the high-efficiency oxygen evolution reaction. *Chem. Soc. Rev.* 50, 8428–8469. <https://doi.org/10.1039/d0cs00962h>.
3. Suen, N.T., Hung, S.F., Quan, Q., Zhang, N., Xu, Y.J., and Chen, H.M. (2017). Electrocatalysis for the oxygen evolution reaction: recent development and future perspectives. *Chem. Soc. Rev.* 46, 337–365. <https://doi.org/10.1039/c6cs00328a>.
4. Huang, Z.F., Song, J.J., Du, Y.H., Xi, S.B., Dou, S., Nsanzimana, J.M.V., Wang, C., Xu, Z.J., and Wang, X. (2019). Chemical and structural origin of lattice oxygen oxidation in Co-Zn oxyhydroxide oxygen evolution electrocatalysts. *Nat. Energy* 4, 329–338. <https://doi.org/10.1038/s41560-019-0355-9>.
5. Grimaud, A., Demortière, A., Saubanère, M., Dachraoui, W., Duchamp, M., Doublet, M.L., and Tarascon, J.M. (2017). Activation of surface oxygen sites on an iridium-based model catalyst for the oxygen evolution reaction. *Nat. Energy* 2, 16189. <https://doi.org/10.1038/energy.2016.189>.
6. Dong, Y., and Komarneni, S. (2021). Strategies to develop earth-abundant heterogeneous oxygen evolution reaction catalysts for pH-neutral or pH-near-neutral electrolytes. *Small Methods* 5, e2000719. <https://doi.org/10.1002/smt.202000719>.
7. Li, P.P., Zhao, R.B., Chen, H.Y., Wang, H.B., Wei, P.P., Huang, H., Liu, Q., Li, T.S., Shi, X.F., Zhang, Y.Y., et al. (2019). Recent advances in the development of water oxidation electrocatalysts at mild pH. *Small* 15, e1805103. <https://doi.org/10.1002/sml.201805103>.
8. Xu, K., Cheng, H., Liu, L.Q., Lv, H.F., Wu, X.J., Wu, C.Z., and Xie, Y. (2017). Promoting active species generation by electrochemical activation in alkaline media for efficient electrocatalytic oxygen evolution in neutral media. *Nano Lett.* 17, 578–583. <https://doi.org/10.1021/acs.nanolett.6b04732>.
9. Song, H.J., Yoon, H., Ju, B., Lee, D.Y., and Kim, D.W. (2020). Electrocatalytic selective oxygen evolution of carbon-coated  $\text{Na}_2\text{Co}_{1-x}\text{Fe}_x\text{P}_2\text{O}_7$  nanoparticles for alkaline seawater electrolysis. *ACS Catal.* 10, 702–709. <https://doi.org/10.1021/acscatal.9b04231>.
10. Zhang, F.H., Yu, L., Wu, L.B., Luo, D., and Ren, Z.F. (2021). Rational design of oxygen evolution reaction catalysts for seawater electrolysis. *Trends Chem.* 3, 485–498. <https://doi.org/10.1016/j.trechm.2021.03.003>.
11. Zhang, L.S., Wang, L.P., Wen, Y.Z., Ni, F.L., Zhang, B., and Peng, H.S. (2020). Boosting neutral water oxidation through surface oxygen modulation. *Adv. Mater.* 32, e2002297. <https://doi.org/10.1002/adma.202002297>.
12. Zhang, L.S., Yuan, H.Y., Wang, L.P., Zhang, H., Zang, Y.J., Tian, Y., Wen, Y.Z., Ni, F.L., Song, H., Wang, H.F., et al. (2020). The critical role of electrochemically activated adsorbates in neutral OER. *Sci. China Mater.* 63, 2509–2516. <https://doi.org/10.1007/s40843-020-1390-6>.
13. Zhang, Y.K., Wu, C.Q., Jiang, H.L., Lin, Y.X., Liu, H.J., He, Q., Chen, S.M., Duan, T., and Song, L. (2018). Atomic iridium incorporated in cobalt hydroxide for efficient oxygen evolution catalysis in neutral electrolyte. *Adv. Mater.* 30, e1707522. <https://doi.org/10.1002/adma.201707522>.
14. Yang, Y., Zhong, H., Yao, G.D., He, R.T., Jin, B.B., and Jin, F.M. (2018). Hydrothermal reduction of  $\text{NaHCO}_3$  into formate with hexahexol. *Catal. Today* 318, 10–14. <https://doi.org/10.1016/j.cattod.2017.09.005>.
15. Zhong, H., Fujii, K., and Nakano, Y. (2017). Effect of  $\text{KHCO}_3$  concentration on electrochemical reduction of  $\text{CO}_2$  on copper

- electrode. *J. Electrochem. Soc.* **164**, F923–F927. <https://doi.org/10.1149/2.0601709jes>.
16. Chen, J., Li, Y.F., Sit, P., and Selloni, A. (2013). Chemical dynamics of the first proton-coupled electron transfer of water oxidation on TiO<sub>2</sub> anatase. *J. Am. Chem. Soc.* **135**, 18774–18777. <https://doi.org/10.1021/ja410685m>.
17. Huynh, M., Bediako, D.K., and Nocera, D.G. (2014). A functionally stable manganese oxide oxygen evolution catalyst in acid. *J. Am. Chem. Soc.* **136**, 6002–6010. <https://doi.org/10.1021/ja413147e>.
18. Tse, E.C.M., Hoang, T.T.H., Varnell, J.A., and Gewirth, A.A. (2016). Observation of an inverse kinetic isotope effect in oxygen evolution electrochemistry. *ACS Catal.* **6**, 5706–5714. <https://doi.org/10.1021/acscatal.6b01170>.
19. Hubert, M.A., Patel, A.M., Gallo, A., Liu, Y.Z., Valle, E., Ben-Naim, M., Sanchez, J., Sokaras, D., Sinclair, R., Nørskov, J.K., et al. (2020). Acidic oxygen evolution reaction activity-stability relationships in Ru-based pyrochlores. *ACS Catal.* **10**, 12182–12196. <https://doi.org/10.1021/acscatal.0c02252>.
20. Kuang, M., Wang, Y., Fang, W., Tan, H.T., Chen, M.X., Yao, J.D., Liu, C.T., Xu, J.W., Zhou, K., and Yan, Q.Y. (2020). Efficient nitrate synthesis via ambient nitrogen oxidation with Ru-doped TiO<sub>2</sub>/RuO<sub>2</sub> electrocatalysts. *Adv. Mater.* **32**, e2002189. <https://doi.org/10.1002/adma.202002189>.
21. Bele, M., Jovanović, P., Marinko, Ž., Drev, S., Selih, V.S., Kovač, J., Gaberšček, M., Koderman Podboršek, G.K., Dražič, G., Hodnik, N., et al. (2020). Increasing the oxygen-evolution reaction performance of nanotubular titanium oxynitride-supported ir nanoparticles by a strong metal-support interaction. *ACS Catal.* **10**, 13688–13700. <https://doi.org/10.1021/acscatal.0c03688>.
22. Cheng, J.F., Yang, J., Kitano, S., Juhasz, G., Higashi, M., Sadakiyo, M., Kato, K., Yoshioka, S., Sugiyama, T., Yamauchi, M., and Nakashima, N. (2019). Impact of Ir-valence control and surface nanostructure on oxygen evolution reaction over a highly efficient Ir-TiO<sub>2</sub> nanorod catalyst. *ACS Catal.* **9**, 6974–6986. <https://doi.org/10.1021/acscatal.9b01438>.
23. An, L., Feng, J.R., Zhang, Y., Zhao, Y.Q., Si, R., Wang, G.C., Cheng, F.Y., Xi, P.X., and Sun, S.H. (2019). Controllable tuning of Fe-N nanosheets by Co substitution for enhanced oxygen evolution reaction. *Nano Energy* **57**, 644–652. <https://doi.org/10.1016/j.nanoen.2018.12.094>.
24. Dileep, N.P., Vineesh, T.V., Sarma, P.V., Chalil, M.V., Prasad, C.S., and Shaijumon, M.M. (2020). Electrochemically exfoliated beta-Co(OH)<sub>2</sub> nanostructures for enhanced oxygen evolution electrocatalysis. *ACS Appl. Energy Mater.* **3**, 1461–1467. <https://doi.org/10.1021/acsaem.9b01901>.
25. Shang, H.S., Sun, W.M., Sui, R., Pei, J.J., Zheng, L.R., Dong, J.C., Jiang, Z.L., Zhou, D.N., Zhuang, Z.B., Chen, W.X., et al. (2020). Engineering isolated Mn-N<sub>2</sub>C<sub>2</sub> atomic interface sites for efficient bifunctional oxygen reduction and evolution reaction. *Nano Lett.* **20**, 5443–5450. <https://doi.org/10.1021/acs.nanolett.0c01925>.
26. Zhang, H.Y., Tian, W.J., Li, Y.G., Sun, H.Q., Tadó, M.O., and Wang, S.B. (2018). A comparative study of metal (Ni, Co, or Mn)-borate catalysts and their photodeposition on rGO/ZnO nanoarrays for photoelectrochemical water splitting. *J. Mater. Chem. A* **6**, 24149–24156. <https://doi.org/10.1039/C8TA06921B>.
27. Shamsipur, M., Taherpour, A.A., and Pashabadi, A. (2018). Comprehensive facilitating of water oxidation reaction by ultrasonic attenuation of hydrogen-bonded structure of water. *Ultrason. Sonochem.* **42**, 381–389. <https://doi.org/10.1016/j.ultrsonch.2017.12.007>.
28. Yang, J.L., Zheng, J.X., Xu, M., Zhuo, Z.Q., Yang, W.L., Wang, L.W., Dai, L.M., Lu, J., Amine, K., and Pan, F. (2018). Short hydrogen bonds on reconstructed nanocrystal surface enhance oxygen evolution activity. *ACS Catal.* **8**, 466–473. <https://doi.org/10.1021/acscatal.7b02814>.
29. Yang, C.P., Hong, C.T., Mai, F.D., Tsai, H.Y., and Liu, Y.C. (2019). Increasing electrochemical reaction rates using treated water with reduced hydrogen bonds. *J. Electroanal. Chem.* **839**, 116–122. <https://doi.org/10.1016/j.jelechem.2019.03.016>.
30. Li, G.F., and Chuang, P.A. (2018). Identifying the forefront of electrocatalytic oxygen evolution reaction: electronic double layer. *Appl. Catal. B* **239**, 425–432. <https://doi.org/10.1016/j.apcatb.2018.08.037>.
31. Barforoush, J.M., Seufferling, T.E., Jantz, D.T., Song, K.R., and Leonard, K.C. (2018). Insights into the active electrocatalytic areas of layered double hydroxide and amorphous nickel-iron oxide oxygen evolution electrocatalysts. *ACS Appl. Energy Mater.* **1**, 1415–1423. <https://doi.org/10.1021/acsaem.8b00190>.
32. Kanan, M.W., and Nocera, D.G. (2008). In situ formation of an oxygen-evolving catalyst in neutral water containing phosphate and Co<sup>2+</sup>. *Science* **321**, 1072–1075. <https://doi.org/10.1126/science.1162018>.
33. Bediako, D.K., Surendranath, Y., and Nocera, D.G. (2013). Mechanistic studies of the oxygen evolution reaction mediated by a nickel-borate thin film electrocatalyst. *J. Am. Chem. Soc.* **135**, 3662–3674. <https://doi.org/10.1021/ja312643z>.
34. Surendranath, Y., Dinca, M., and Nocera, D.G. (2009). Electrolyte-dependent electrosynthesis and activity of cobalt-based water oxidation catalysts. *J. Am. Chem. Soc.* **131**, 2615–2620. <https://doi.org/10.1021/ja807769r>.
35. Li, C.F., Zhao, J.W., Xie, L.J., Wu, J.Q., Ren, Q., Wang, Y., and Li, G.R. (2021). Surface-adsorbed carboxylate ligands on layered double hydroxides/metal-organic frameworks promote the electrocatalytic oxygen evolution reaction. *Angew. Chem. Int. Ed. Engl.* **60**, 18129–18137. <https://doi.org/10.1002/anie.202104148>.
36. Shi, Y.M., Du, W., Zhou, W., Wang, C.H., Lu, S.S., Lu, S.Y., and Zhang, B. (2020). Unveiling the promotion of surface-adsorbed Chalcogenate on the electrocatalytic oxygen evolution reaction. *Angew. Chem. Int. Ed. Engl.* **59**, 22470–22474. <https://doi.org/10.1002/anie.202011097>.
37. Hunter, B.M., Hieringer, W., Winkler, J.R., Gray, H.B., and Müller, A.M. (2016). Effect of interlayer anions on [NiFe]-LDH nanosheet water oxidation activity. *Energy Environ. Sci.* **9**, 1734–1743. <https://doi.org/10.1039/C6EE00377J>.
38. Tang, S., Li, X., Courté, M., Peng, J., and Fichou, D. (2020). Hierarchical Cu(OH)<sub>2</sub>@Co(OH)<sub>2</sub> nanotrees for water oxidation electrolysis. *ChemCatChem* **12**, 4038–4043. <https://doi.org/10.1002/cctc.202000558>.
39. Ge, A.M., Videla, P.E., Lee, G.L., Rudshyeyn, B., Song, J., Kubiak, C.P., Batista, V.S., and Lian, T.Q. (2017). Interfacial structure and electric field probed by in situ electrochemical vibrational stark effect spectroscopy and computational modeling. *J. Phys. Chem. C* **121**, 18674–18682. <https://doi.org/10.1021/acs.jpcc.7b05563>.
40. Schkolnik, G., Salewski, J., Millo, D., Zebger, I., Franzen, S., and Hildebrandt, P. (2012). Vibrational stark effect of the electric-field reporter 4-Mercaptobenzonitrile as a tool for investigating electrostatics at electrode/SAM/solution interfaces. *Int. J. Mol. Sci.* **13**, 7466–7482. <https://doi.org/10.3390/ijms13067466>.
41. Yeo, B.S., Klaus, S.L., Ross, P.N., Mathies, R.A., and Bell, A.T. (2010). Identification of hydroperoxy species as reaction intermediates in the electrochemical evolution of oxygen on gold. *ChemPhysChem* **11**, 1854–1857. <https://doi.org/10.1002/cphc.201000294>.
42. Yeo, B.S., and Bell, A.T. (2011). Enhanced activity of gold-supported cobalt oxide for the electrochemical evolution of oxygen. *J. Am. Chem. Soc.* **133**, 5587–5593. <https://doi.org/10.1021/ja200559j>.